




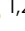


## Dynamical and topological properties of the spin angular momenta in general electromagnetic fields

Peng Shi <sup>1</sup>, Luping Du <sup>1</sup>, Aiping Yang<sup>1</sup>, Xiaojin Yin<sup>1</sup>, Xinrui Lei<sup>1</sup> & Xiacong Yuan <sup>1,2</sup>

Spin angular momenta play important roles in light-matter interactions, leading to the emergence of the spin Hall effect and topological quasiparticles in modern optics. The typical approach is to decompose the spins of plane electromagnetic waves into longitudinal and transverse components, yet this description is not easily transferable to more structured electromagnetic environments. Here, we developed a field theory to reveal the physical origin and topological properties of longitudinal and transverse spins for arbitrary electromagnetic waves (including water waves and acoustic waves) in both near-field and free space. For electromagnetic waves carrying intrinsic helicity, we observed the emergence of helicity-dependent transverse spin possessing helicity-dependent spin-momentum locking. To verify that the number of spin-momentum locking states coincides with the spin Chern number, we experimentally measured the three-dimensional spin angular momentum densities of Bloch-type optical skyrmions. Our findings yield valuable insight for constructing spin-based field theory and exploiting optical topological quasiparticle-based applications.

<sup>1</sup>Nanophotonics Research Centre, Institute of Microscale Optoelectronics & State Key Laboratory of Radio Frequency Heterogeneous Integration, Shenzhen University, Shenzhen 518060, China. <sup>2</sup>Zhejiang Lab, Research Center for Humanoid Sensing, Research Institute of Intelligent Sensing, Hangzhou 311100, China. ✉email: [pittshiustc@gmail.com](mailto:pittshiustc@gmail.com); [lpdu@szu.edu.cn](mailto:lpdu@szu.edu.cn); [xcyuan@szu.edu.cn](mailto:xcyuan@szu.edu.cn)

Momentum and angular momentum are fundamental dynamical properties of elementary particles and waves and play important roles in understanding the behaviours arising from wave–matter interactions<sup>1–7</sup>. In classical electromagnetic (EM) fields, the angular momentum can be divided into spin angular momentum (SAM) associated with the degree of circular polarization and orbital angular momentum (OAM) related to the phase singularity. Recently, it was discovered that, for a plane-wave solution of Maxwell’s equations, the EM helicity-dependent SAM component oriented along the mean wavevector (canonical momentum  $\mathbf{P}$ ) was considered a longitudinal spin (L-spin)<sup>2</sup>, whereas the SAM components oriented perpendicular to the mean wavevector represented the helicity-independent transverse spins (T-spin)<sup>8</sup>. To date, the helicity-independent T-spins have been investigated in various EM systems, including focused fields<sup>9,10</sup>, interference fields<sup>11</sup>, evanescent fields<sup>12–15</sup>, guided fields<sup>16,17</sup> and unpolarized fields<sup>18</sup>. The SAM interacts intensively with OAM<sup>19</sup>, especially on the subwavelength scale, raising strong research interest in spin–orbit interactions (SOIs) and other remarkable phenomena<sup>20–27</sup> and offering potential applications in the fields of angular-momentum-based optical manipulation<sup>28,29</sup>, unidirectional guided waves<sup>30–33</sup>, imaging<sup>34–36</sup>, detection and nanometrology<sup>37,38</sup>, and on-chip quantum technologies<sup>39</sup>.

However, if complicated structural properties<sup>40</sup>, including the inhomogeneities of the intensity, phase, polarization and helicity, are introduced into the EM fields, distinguishing between L-spins and T-spins in the empirical wavevector approach (i.e., longitudinal/transverse meaning parallel/perpendicular to the canonical momentum) brings physical challenges. Moreover, it is ambiguous when the decomposition of the total SAM into the L-spin and T-spin is based on their direction of vector instead of their physical difference. This ambiguity emerges because an arbitrary structured EM field can possess three-dimensional (3D) distributions of spin angular momentum density. Previously, some researchers proposed that T-spins possess the property of spin-momentum locking<sup>13</sup>. However, such a proposal is based on a single evanescent wave. Soon afterwards, these researchers presented diversified expressions to describe the T-spins for different EM systems<sup>28</sup>. These expressions are intriguing because from the physical point of view, a class of physical quantities should possess a unified physical mechanism embodied by a single universal equation. In quantum physics, photons are spin-1 bosons<sup>41</sup>, and hence, it is reasonable to extract the L-spin correspondence using concepts in quantum physics. However, for a generic EM field, the physical origin of T-spins and their properties await quantitative elucidation. For other diverse classical wave fields, such as acoustic and gravity water waves, the mediating phonons are spin-0 phonons and hence should not possess L-spin. However, both wave fields definitely carry SAMs<sup>6</sup>. These helicity-independent SAMs correspond to the T-spin of a helicity-independent linearly polarized EM field<sup>17</sup> and have the same physical origin and possess unified physical properties.

In this study, we constructed a unified field theory based on the decomposition of the SAM for a generic interfering EM field into L-spins and T-spins, which enables their physical origins and accompanying intrinsic topological properties to be uncovered. The decomposition technique can be applied to spin decompositions for diversified classical wave fields, including acoustic and gravity water waves. The equations reveal that L-spins are associated with the helicity that is oriented parallel to the local wavevector given by the Minkowski-type canonical momentum<sup>42–45</sup>, whereas T-spins stem from the inhomogeneity of the kinetic Abraham momentum density<sup>42–45</sup> of the field and locks with the kinetic Abraham momentum in the near field or free space. Here, the Minkowski-type canonical momentum is

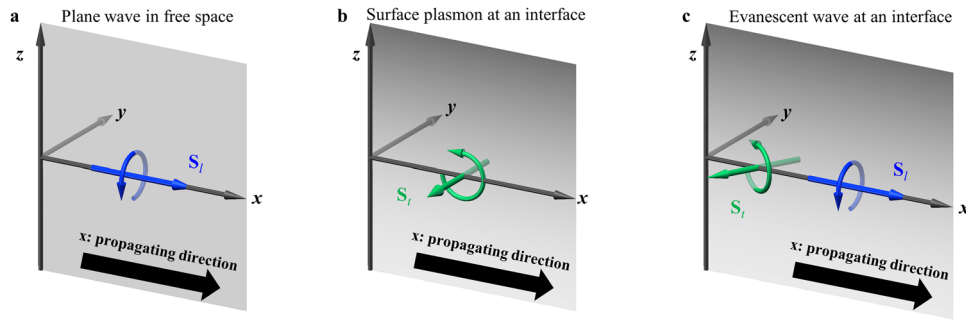
related to the quantum momentum operator, and the Abraham kinetic momentum is related to the relativistic transportation of photons and determined by the group velocity. If an inhomogeneity of the helicity-related kinetic momentum density is present in a structured EM field, a helicity-dependent T-spin appears and simultaneously leads to helicity-dependent spin-momentum locking. Under this circumstance, the number of spin-momentum locking states is consistent with the nontrivial topological spin Chern number of the EM field. In addition, the helicity-dependent T-spin refers to the inverted helical component in the EM system and therefore is closely related to the evolution of the geometric phase in optical systems. More curiously, this decomposition of the spin vector results in a kind of T-spin oriented parallel to the mean wavevector and L-spin oriented perpendicular to the mean wavevector, which demonstrates that the empirical wavevector approach definitely faces challenges in separating the L-spins and T-spins of structured light fields. By this theory, we theoretically deduced that a Bloch-type optical skyrmion will be present in free space. Furthermore, we experimentally demonstrated the spin properties of this Bloch-type optical skyrmion by mapping the three SAM components in an optical focused beam with circular polarizations in our in-house developed near-field imaging system. Our findings deepen the understanding of the underlying physics of spins for classical wave fields and open an avenue for applications including optical manipulations and data storage.

## Results

**Basic concepts of the EM longitudinal and transverse spin.** In quantum physics, photons are spin-1 bosons with the direction of spin parallel to that of the photon momentum<sup>41</sup>. To determine the physical properties of L-spins in a classical EM field, we first took an elliptically polarized plane wave propagating in the  $x$ -direction with electric and magnetic fields [Fig. 1(a)]

$$\begin{aligned} \mathbf{E}(\mathbf{r}) &= (+A_s \hat{\mathbf{y}} + A_p \hat{\mathbf{z}}) \exp[i(kx - \omega t)] \text{ and} \\ \mathbf{H}(\mathbf{r}) &= \left( -\frac{A_p}{\eta} \hat{\mathbf{y}} + \frac{A_s}{\eta} \hat{\mathbf{z}} \right) \exp[i(kx - \omega t)] \end{aligned} \quad (1)$$

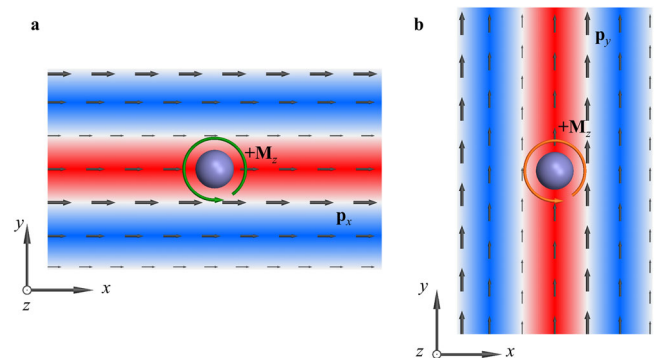
defined in arbitrary orthogonal coordinates  $(x, y, z)$ . Here, the total SAM density of this plane wave is  $\mathbf{S} = \hbar \sigma \hat{\mathbf{k}}$ , where  $\sigma = \text{Im}\{A_s^* A_p - A_p^* A_s\} / \{A_s^* A_s + A_p^* A_p\}$  is the helicity of a single wave packet (in accordance with the Stokes parameter  $s_3$  and termed the polarization ellipticity<sup>11,28</sup>) and  $\hat{\mathbf{k}}$  is only related to the canonical momentum density  $\mathbf{P}$  by  $\hat{\mathbf{k}} = \mathbf{P} / \hbar k$  but is not the unit directional vector (Supplementary Note 1). Moreover,  $A_s$  and  $A_p$  denote the amplitudes of the  $s$ -polarization and  $p$ -polarization, respectively;  $\eta = \sqrt{\mu/\epsilon}$  is the wave impedance;  $\hbar$  is the reduced Planck constant;  $\omega$  is the angular frequency; and  $k$  is the wavenumber. The special instances  $\sigma = \pm 1$  represent the two circularly polarized (CP) modes of light corresponding to the two helical states in quantum physics<sup>2,26–28,41</sup>. Thus, the expression for the SAM helps delineate the global properties of EM fields from the perspective of classical field theory as well as the elementary dynamical properties of optical wave packets from the viewpoint of quantum theory. The spin vector of CP light is parallel to the local wavevector density  $\hat{\mathbf{k}}$  and thus was previously regarded as L-spin. In physics, for theoretical consistency, the elementary feature of L-spins in a generic EM field should coincide with the definition of the photonic spin in quantum physics, i.e., the L-spin is parallel to the local wavevector density  $\hat{\mathbf{k}}$ , and its magnitude and sign are determined by the helicity  $\sigma$  of the EM field.



**Fig. 1 Spin and momentum properties of a plane wave in free space, a surface plasmon plane wave at a metal/dielectric interface and a single evanescent wave at an interface.** For (a) an elliptically polarized plane wave propagating in the  $x$ -direction, the kinetic momentum density  $\mathbf{\Pi}$  is equal to the canonical momentum density  $\mathbf{P}$ , and the whole SAM ( $\mathbf{S}$ ) is the L-spin ( $\mathbf{S}_l$ ), which is homogeneous through the space; for (b) a linearly polarized surface plasmon plane wave<sup>17</sup> propagating in the  $x$ -direction, the kinetic momentum density  $\mathbf{\Pi}$  and the canonical momentum density  $\mathbf{P}$  are paralleled with the spin momentum along the  $x$ -direction, and the whole SAM is the T-spin ( $\mathbf{S}_t$ ), which decays exponentially along the  $+z$ -direction; for (c) a single evanescent wave, the canonical momentum density  $\mathbf{P}$  is along the  $x$ -direction, whereas the spin momentum density  $\mathbf{P}_s = \nabla \times \mathbf{S}/2$  has an  $x$ -component and  $y$ -component because the SAM density contains an L-spin and T-spin simultaneously and these spins decay exponentially along the  $+z$ -direction. Therefore, the kinetic momentum density  $\mathbf{\Pi}$  also has an  $x$ -component and  $y$ -component simultaneously.

On the other hand, to uncover the physical origin of T-spin, we considered a classical hydrodynamic model in which a particle is immersed in a fluid possessing a gradient field of momentum [Fig. 2]. Assuming the flow of the water wave is in the  $+x$ -direction with its momentum density decreasing in the  $y$ -direction, the immersed particle experiences an anticlockwise transverse torque ( $M_z$ ), and its intensity is proportional to the local gradient of the momentum density in the  $y$ -direction [Fig. 2(a)]. If the flow is in the  $+y$ -direction with momentum density increasing in the  $x$ -direction, the immersed particle also experiences an anticlockwise transverse torque ( $M_z$ ) with an intensity proportional to the local gradient of momentum density in the  $x$ -direction [Fig. 2(b)]. In total, the particle immersed in the fluid flow with a gradient momentum density experiences a transverse torque, the intensity of which is proportional to the vorticity associated with the momentum density. This model is also available if the generation of T-spins is considered for the linearly polarized surface plasmon plane wave, as shown in Fig. 1(b), because the three momentum densities, including the kinetic, canonical and spin momentum densities<sup>2,26–28,42–45</sup>, decay exponentially along the  $+z$ -direction. Correspondingly, we conjectured that the generation of T-spins in an EM system is related to the vorticity associated with the momentum flow of the photons.

In classical field theory, there are three types of momentum densities:<sup>6,46</sup> the Abraham kinetic momentum density  $\mathbf{\Pi}$  of photons or phonons associated with the Poynting vectors of wave fields, which can be decomposed into the Minkowski-type canonical momentum density  $\mathbf{P}$  and the Belinfante spin momentum density  $\mathbf{P}_s$ . These three momentum densities describing the flows (group velocities) of photons<sup>47</sup> or phonons<sup>6</sup> are candidates for evaluating T-spin. Previously, for plane waves of an EM system, only the canonical momentum  $\mathbf{P}$  associated with the local wavevector was employed to identify the T-spin in various ways<sup>28</sup>. However, for these diverse classical wave fields, basic physical challenges are faced when searching for a unified physical mechanism to evaluate T-spins in a universal manner because the spin momentum density  $\mathbf{P}_s$  appears to also play a critical role in the generation of T-spins. For example, for plane waves of an EM field that has a pure L-spin ( $\mathbf{S} \parallel \hat{\mathbf{k}}$ ), if the spin momentum density  $\mathbf{P}_s = \nabla \times \mathbf{S}/2$  exists, it would be perpendicular to the wavevector  $\hat{\mathbf{k}}$  ( $\mathbf{P}_s \perp \hat{\mathbf{k}}$ ). This is illogical because spin momentum density should also be longitudinal; thus,  $\mathbf{P}_s$  vanishes for the field with pure L-spin. In contrast, for an inhomogeneous



**Fig. 2 A hydrodynamic model is used to reveal the relationship between the transverse torque  $M_z$  and momentum flow.** a The momentum flow propagating along the  $+x$ -direction with the magnitude gradually decreasing in the  $y$ -direction causes the immersed particle to rotate anticlockwise; and (b) the momentum flow propagating along the  $+y$ -direction with the magnitude gradually increasing in the  $x$ -direction also causes the Rayleigh particle to rotate anticlockwise. The overall spinning effect on the immersed particle is therefore related to the vorticity of the momentum flow. This theoretical analysis is consistent with the spin-momentum relation of deep-water gravity waves:  $\mathbf{S}_{\text{GW}} = \nabla_2 \times \mathbf{\Pi}_{\text{GW}}/2k_{\text{GW}}^2$ . The magnitude of each arrow indicates the intensity of the momentum flow, and the direction of the momentum flow is given by the arrow's orientation. The background colour indicates the  $z$ -component SAM density, with red and blue indicating the positive and negative SAM densities, respectively.

structured EM field containing T-spins [Fig. 1(b) and (c)], the spin momentum density  $\mathbf{P}_s = \nabla \times \mathbf{S}/2$  would contain the longitudinal component (for example, the spin momentum density of a single evanescent wave contains longitudinal and transverse components simultaneously<sup>12</sup>). This is prevalent in a structured field, and thus, the spin momentum is closely connected with the T-spin. In particular, for a relativistic field such as an EM wave, the canonical group velocity determined by the canonical momentum would be superluminal<sup>47</sup>. This contradicts a principle of relativity, and hence, a spin momentum should appear and be antiparallel to the canonical momentum to guarantee that the total group velocity associated with the kinetic momentum is subluminal<sup>47</sup>. In other words, spin momentum is essential and highly related to the T-spin in a structured field, and therefore, the kinetic momentum, which combines canonical and

spin momenta, is reasonable when employed to evaluate the T-spin in general scenarios.

**Field theory for the EM longitudinal and transverse spins.** For a general structured EM wave carrying helicity and inhomogeneities simultaneously, we theoretically proved that the T-spin ( $\mathbf{S}_t$ ) and L-spin ( $\mathbf{S}_l$ ) of an arbitrary EM wave can be determined by (Supplementary Notes 2, 3)

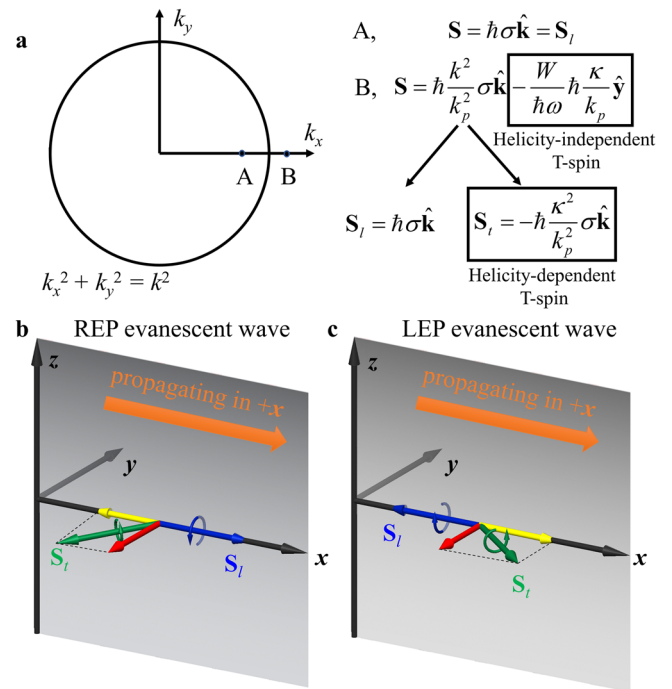
$$\mathbf{S}_l = \sum_i \hbar \sigma_i \hat{\mathbf{k}}_i + \sum_{i \neq j} \hbar \sigma_{ij} \hat{\mathbf{k}}_{ij}, \quad (2)$$

and

$$\mathbf{S}_t = \frac{1}{2k^2} \nabla \times \Pi. \quad (3)$$

Here, we considered a generic EM field for which the electric and magnetic field components can be expanded into the superpositions of a plane-wave basis and carry the helicity  $\sigma_i$  and local wavevector  $\hat{\mathbf{k}}_i$  for each elementary plane wave  $i$  and the helicity  $\sigma_{ij}$  and local wavevector  $\hat{\mathbf{k}}_{ij}$  for the coupling of the interfering plane waves  $i$  and  $j$ . We must emphasize that the coupling term  $\hbar \sigma_{ij} \hat{\mathbf{k}}_{ij}$  appears for the non-orthogonality of the plane-wave basis, which can be widely found in focused structured light. For example, the focused Laguerre-Gaussian (LG) beam carrying OAM but without EM helicity can result in an L-spin<sup>48–51</sup>. The total spin is thus given by  $\mathbf{S} = \mathbf{S}_l + \mathbf{S}_t = \langle \psi | \hat{\mathbf{S}} | \psi \rangle / \hbar \omega$  and  $\hat{\mathbf{S}} = [\hat{\mathbf{S}}, \mathbf{0}; \mathbf{0}, \hat{\mathbf{S}}]$ , with  $\hat{\mathbf{S}}$  representing the spin-1 matrix in  $SO(3)$ <sup>46</sup>,  $\mathbf{0}$  representing the  $3 \times 3$  zero matrix, and  $|\psi\rangle$  representing the Riemann–Silberstein vector, which can be considered the photon wave function analogous to the quantum wave function<sup>46</sup>. Notably, the L-spin is based on the link between the EM helicities  $\sigma_i$  for each of the elementary interfering waves and their local wavevectors  $\hat{\mathbf{k}}_i$  rather than the mean wavevector. In our work, the mean wavevector is given by the canonical momentum of the total EM field, whereas the local wavevector is identified by the canonical momentum of each plane-wave component when expanding the EM field into a superposition of plane waves. Thus, the first term on the right side of Eq. (2) represents the summation of L-spins of each elementary plane wave, and the second term represents the sum of L-spins from couplings between the interfering plane waves. The appearance of the coupling term stems from the non-orthogonality of the two plane-wave basis in the 3D polarization space.

On the other hand, Eq. (3) reveals that for an EM wave, the T-spin arises from the inhomogeneous momentum flow density of the EM field. Moreover, the T-spin is locked to the kinetic momentum<sup>13–17</sup> in a manner unrelated to the L-spin of the EM wave propagating in a homogeneous medium. This spin-momentum locking originates from the intrinsic spin-orbit coupling in Maxwell's equations and is considered a fundamental property of the T-spin for an arbitrary EM field, either propagating in free space or confined at an interface (evanescent and surface waves). Moreover, because of the long-standing Abraham–Minkowski debate<sup>42–45</sup>, the accepted wisdom is that the Minkowski-type canonical momentum determines the local wavevector of photons and is reasonable for evaluating the L-spin, whereas the Abraham kinetic momentum is always associated with the group velocities and describes the current properties of EM wave fields (called a current by M.V. Berry<sup>46</sup>). Therefore, spin-momentum locking between the kinetic momentum and SAM can also be regarded as spin-current locking and thus is different from the quantum spin-Hall effect in condensed matter physics<sup>52</sup>. In addition, from the  $PT$ -symmetric point of view, the angular momentum given by  $\mathbf{L} = \mathbf{r} \times \mathbf{P}$  is  $P$ -even and  $T$ -



**Fig. 3 Spin decomposition of an elliptically polarized plane wave.**

**a**  $k$ -space representation of the plane waves, in which the wavenumbers confined within the circle  $k_x^2 + k_y^2 = k^2$  correspond to waves propagating in free space, whereas those outside the circle correspond to a single evanescent wave confined to an interface. The consistency of the elementary feature of L-spin for the same kind of wave-packets (Points “A” and “B”) leads to the classification of the T-spin into the normal helicity-independent component aligned perpendicular to the wavevector (the  $y$ -component) and the helicity-dependent component aligned anti-parallel to the wavevector. **b, c** Illustrations of the generic spin properties of right-handed and left-handed elliptically polarized evanescent waves propagating along the  $+x$ -direction. If the kinetic momentum is reversed, the T-spins (green arrows), including the helicity-independent T-spin (red arrows) and the helicity-dependent T-spin (yellow arrows), become opposite. Therefore, four spin-momentum locking states exist in a general EM system, consistent with the  $\mathbb{Z}_4$  topological invariance of the optical wave packet<sup>17</sup>.

odd because the position vector  $\mathbf{r}$  is  $P$ -odd and  $T$ -even, whereas the momentum vector  $\mathbf{P}$  is  $P$ -odd and  $T$ -odd. Regarding the L-spin given by Eq. (2), the helicity  $\sigma$  is  $P$ -odd and  $T$ -even, whereas the unit vector of the local wavevector  $\hat{\mathbf{k}}$ , which possesses properties in accordance with the momentum ( $\mathbf{P} = \hbar k \hat{\mathbf{k}}$ ), is  $P$ -odd and  $T$ -odd. Therefore, the L-spin  $\mathbf{S}_l$  is also  $P$  even and  $T$  odd. Regarding the T-spin given by Eq. (3), the kinetic momentum is  $P$ -odd and  $T$ -odd, and the gradient operator  $\nabla$  is  $P$ -odd and  $T$ -even; thus, the angular momentum  $\mathbf{S}_t$  is also  $P$ -even and  $T$ -odd.

**Helicity-dependent and spin-momentum locking properties of the EM spins.** To further understand the decomposition of the spins of complex EM fields into L-spins and T-spins using our theory, we still considered an elliptically polarized plane wave. A plane wave either propagates or evanesces depending on the wavevector components [Fig. 3(a)]. If the wave is propagating along the  $x$ -direction, for a plane wave in free space, as demonstrated in Eq. (1) [Point “A” in Fig. 3(a)], the SAM of the wave is  $\mathbf{S} = \hbar \sigma \hat{\mathbf{k}}$  and is pure L-spin, as analysed in Fig. 1(a). We now consider its evanescent counterpart [point “B” in Fig. 3(a)] with

the following electric and magnetic fields:

$$\begin{aligned} \mathbf{E}(\mathbf{r}) &= \left( -A_p \frac{i\kappa}{k} \hat{\mathbf{x}} + A_s \hat{\mathbf{y}} + \frac{A_p k_p}{k} \hat{\mathbf{z}} \right) e^{i(k_p x - \kappa z)} \text{ and} \\ \mathbf{H}(\mathbf{r}) &= \left( -A_s \frac{i\kappa}{k\eta} \hat{\mathbf{x}} - \frac{A_p}{\eta} \hat{\mathbf{y}} + \frac{A_s k_p}{k\eta} \hat{\mathbf{z}} \right) e^{i(k_p x - \kappa z)}. \end{aligned} \quad (4)$$

The SAM is found to be

$$\mathbf{S} = \frac{W}{\omega} \frac{\kappa}{k_p} \left( \frac{k}{\kappa} \sigma \hat{\mathbf{x}} - 1 \hat{\mathbf{y}} \right) = \frac{k^2}{k_p^2} \hbar \sigma \hat{\mathbf{k}} - \frac{W}{\omega} \frac{\kappa}{k_p} \hat{\mathbf{y}}, \quad (5)$$

where  $k_p$  denotes the horizontal wavenumber,  $i\kappa$  represents the wavenumber in the  $z$ -direction with  $k_p^2 = k^2 + \kappa^2$ , and  $W$  denotes the time-averaged energy density. We observed that the  $y$ -component of the SAM corresponds to the normal helicity-independent T-spin of a linearly polarized surface plane wave (transverse magnetic (TM) or transverse electric (TE) polarization)<sup>17</sup> and is perpendicular to the local wavevector  $\hat{\mathbf{k}}$ . However, compared with the EM helicity of a propagating elliptically polarized plane wave, the SAM component parallel to the local wavevector contains an additional factor:  $k^2/k_p^2$ , which is illogical in physics if we consider it entirely as an L-spin because the elementary feature of the L-spin for the same kind of wavepacket should be constant [Fig. 3(a)]. Indeed, given the evanescent property of the wave in the  $z$ -direction, we determined that the kinetic momentum density contains two components:

$$\mathbf{\Pi} = \frac{W}{c} \frac{k}{k_p} \left( 1 \hat{\mathbf{x}} - \frac{\kappa}{k} \sigma \hat{\mathbf{y}} \right) = \hbar \frac{k^3}{k_p^2} \left( 1 \hat{\mathbf{k}} - \frac{W}{\hbar \omega} \frac{\kappa k_p}{k^2} \sigma \hat{\mathbf{y}} \right), \quad (6)$$

where the helicity-unrelated  $x$ -component of the momentum and the helicity-related  $y$ -component of the momentum density both decay in the  $z$ -direction. Thus, we can expect two components of the T-spin as follows:

$$\mathbf{S}_t = \frac{1}{2k^2} \nabla \times \mathbf{\Pi} = \frac{W}{\omega} \frac{\kappa}{k_p} \left( -\frac{\kappa}{k} \sigma \hat{\mathbf{x}} - 1 \hat{\mathbf{y}} \right) = -\hbar \frac{\kappa^2}{k_p^2} \sigma \hat{\mathbf{k}} - \frac{W}{\omega} \frac{\kappa}{k_p} \hat{\mathbf{y}}, \quad (7)$$

whereas the L-spin is  $\mathbf{S}_l = \mathbf{S} - \mathbf{S}_t = \hbar \sigma \hat{\mathbf{k}}$ , which now coincides with that in free space. Aside from the helicity-independent T-spin that was investigated intensively in the past<sup>8–18</sup>, a hidden T-spin that is helicity-dependent is predicted from the theory. This leads to four spin-momentum locking states for a generic EM field [Fig. 3(b, c)], in which the respective spin properties of the right-handed and left-handed elliptically polarized states propagating in the  $+x$ -direction are shown. If the kinetic momentum associated with the flow of photons is reversed, both the helicity-dependent and helicity-independent T-spins are inverted simultaneously. This indicates that the general EM field possesses  $\mathbb{Z}_4$  topological invariance, which is consistent with the nontrivial spin Chern number of photons<sup>17</sup>. When the dual symmetry between the electric and magnetic constitutive relations is broken<sup>53</sup> and only a linearly polarized state survives, the four spin-momentum locking states downgrade to two helicity-independent states, which are similar to the quantum spin Hall effect of light proposed by Ref. 13

The aforementioned concepts of EM spin can be generalized to an arbitrary EM wave field by expanding it into the superposition of plane waves for either near field or free space. In this study, for simplicity, we only demonstrated two-wave interference of the single evanescent waves as an example [Fig. 4(a, d, g)]. The results can be extended to multiple wave interference and thus an

arbitrary EM field. We assume that the two interfering fields are

$$\begin{aligned} \mathbf{E}_1(\mathbf{r}) &= \left( -\frac{A_{p1} i\kappa}{k} \hat{\mathbf{x}} + A_{s1} \hat{\mathbf{y}} + \frac{A_{p1} k_p}{k} \hat{\mathbf{z}} \right) e^{i(k_p x - \kappa z)} \text{ and} \\ \mathbf{E}_2(\mathbf{r}) &= \left( -\frac{A_{p2} i\kappa}{k} \hat{\mathbf{x}} + A_{s2} \hat{\mathbf{y}} + \frac{A_{p2} k_p}{k} \hat{\mathbf{z}} \right) e^{i(k_p x - \kappa z)} \end{aligned} \quad (8)$$

and are rotated through angles  $+\theta$  and  $-\theta$  with respect to the  $x$ -axis.  $A_{p1}/A_{p2}$  and  $A_{s1}/A_{s2}$  represent the amplitude of wave 1/2, respectively. Then, the total electric field of the superposed field is expressible as

$$\mathbf{E} = \hat{R}_z(-\theta) \mathbf{E}_1[\hat{R}_z(\theta) \mathbf{r}] + \hat{R}_z(\theta) \mathbf{E}_2[\hat{R}_z(-\theta) \mathbf{r}], \quad (9)$$

Here,  $\hat{R}_z(\theta)$  denotes the rotational operator with respect to the  $z$ -axis, and  $r = (x, y, z)$  represents the coordinates. The magnetic field is calculated using Faraday's law of electromagnetic induction,  $\mathbf{H} = \nabla \times \mathbf{E}/i\omega\mu$ . We can then obtain an energy density containing three parts  $W = W_1 + W_2 + W_c$ , for which

$$\begin{aligned} W_1 &= \frac{\epsilon k_p^2}{2k^2} \{A_{p1}^* A_{p1} + A_{s1}^* A_{s1}\} e^{-2\kappa z} \text{ and} \\ W_2 &= \frac{\epsilon k_p^2}{2k^2} \{A_{p2}^* A_{p2} + A_{s2}^* A_{s2}\} e^{-2\kappa z} \end{aligned} \quad (10)$$

denote the energy densities of Waves 1 and 2, and

$$\begin{aligned} W_c &= \frac{\epsilon k_p^2}{2k^2} \{ (A_{p1}^* A_{p2} e^{-2ik_{s1}y} + A_{p2}^* A_{p1} e^{+2ik_{s1}y}) \\ &\quad + (A_{s1}^* A_{s2} e^{-2ik_{s1}y} + A_{s2}^* A_{s1} e^{+2ik_{s1}y}) \} e^{-2\kappa z} \end{aligned} \quad (11)$$

denotes the coupling energy density with  $k_{s1} = k_p \sin\theta$  and  $k_{p1} = k_p \cos\theta$ .  $W_1/W_2$  denotes the energy density of Wave 1/2. Here,  $W_c$  is local, and its integral over the whole  $xy$ -plane vanishes. Based on this decomposition of the energy density, the mean wavevector of the superposed field is also decomposable to  $\hat{\mathbf{k}} = \hat{\mathbf{k}}_1 + \hat{\mathbf{k}}_2 + \hat{\mathbf{k}}_c$ , for which the local wavevectors of Waves 1 and 2 are

$$\hat{\mathbf{k}}_1 = \frac{W_1}{\hbar \omega} \left( \frac{k_{p1}}{k_p} \hat{\mathbf{x}} + \frac{k_{s1}}{k_p} \hat{\mathbf{y}} \right) \text{ and } \hat{\mathbf{k}}_2 = \frac{W_2}{\hbar \omega} \left( \frac{k_{p1}}{k_p} \hat{\mathbf{x}} - \frac{k_{s1}}{k_p} \hat{\mathbf{y}} \right), \quad (12)$$

and

$$\hat{\mathbf{k}}_c = \frac{W_c}{\hbar \omega} \left( \frac{k_{p1}}{k_p} \hat{\mathbf{x}} \right) \quad (13)$$

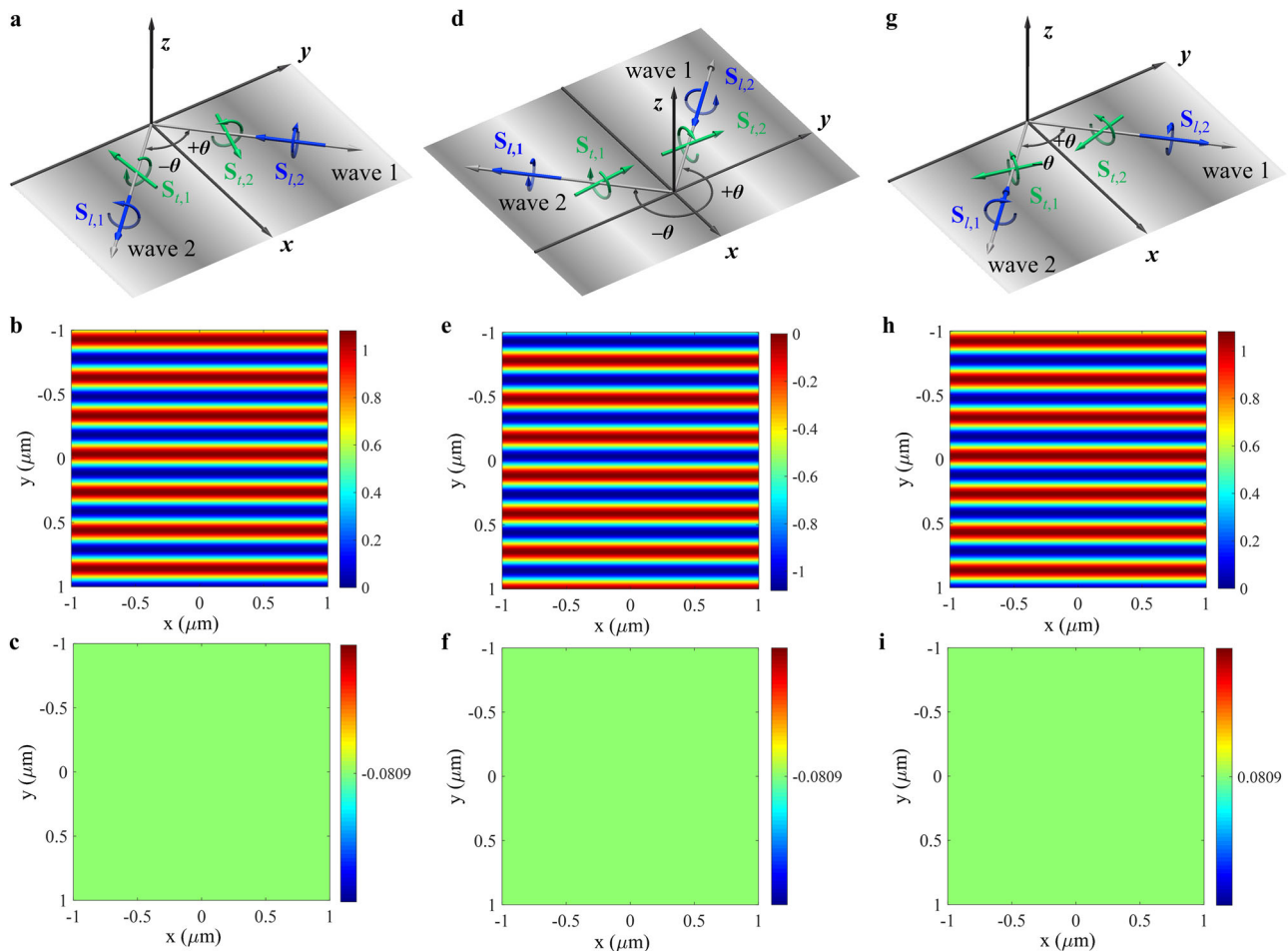
represents the local wavevector of the coupling energy density by comparing the total energy density and mean wavevector of the superposed field. In this way, the L-spin can be rewritten as  $\mathbf{S}_l = \hbar \sigma_1 \hat{\mathbf{k}}_1 + \hbar \sigma_2 \hat{\mathbf{k}}_2 + \hbar \sigma_c \hat{\mathbf{k}}_c$ , where the three helicities are

$$\sigma_1 = \frac{\text{Im}\{A_{s1}^* A_{p1} - A_{s1} A_{p1}^*\}}{A_{p1}^* A_{p1} + A_{s1}^* A_{s1}} \text{ and } \sigma_2 = \frac{\text{Im}\{A_{s2}^* A_{p2} - A_{s2} A_{p2}^*\}}{A_{p2}^* A_{p2} + A_{s2}^* A_{s2}}, \quad (14)$$

and

$$\sigma_c = \frac{\text{Im}\{(A_{s1}^* A_{p2} e^{-2ik_{s1}y} - A_{s1} A_{p2}^* e^{+2ik_{s1}y}) + (A_{s2}^* A_{p1} e^{+2ik_{s1}y} - A_{s2} A_{p1}^* e^{-2ik_{s1}y})\}}{(A_{p1}^* A_{p2} e^{-2ik_{s1}y} + A_{p2}^* A_{p1} e^{+2ik_{s1}y}) + (A_{s1}^* A_{s2} e^{-2ik_{s1}y} + A_{s2}^* A_{s1} e^{+2ik_{s1}y})}, \quad (15)$$

respectively. The helicity of each individual wave is given by the corresponding polarization ellipticity<sup>11,28</sup>. Thus, the link between the EM helicities and their local wavevectors is intrinsically based on the decomposition of the energy density and mean wavevector. The same conclusion can be reached for waves in



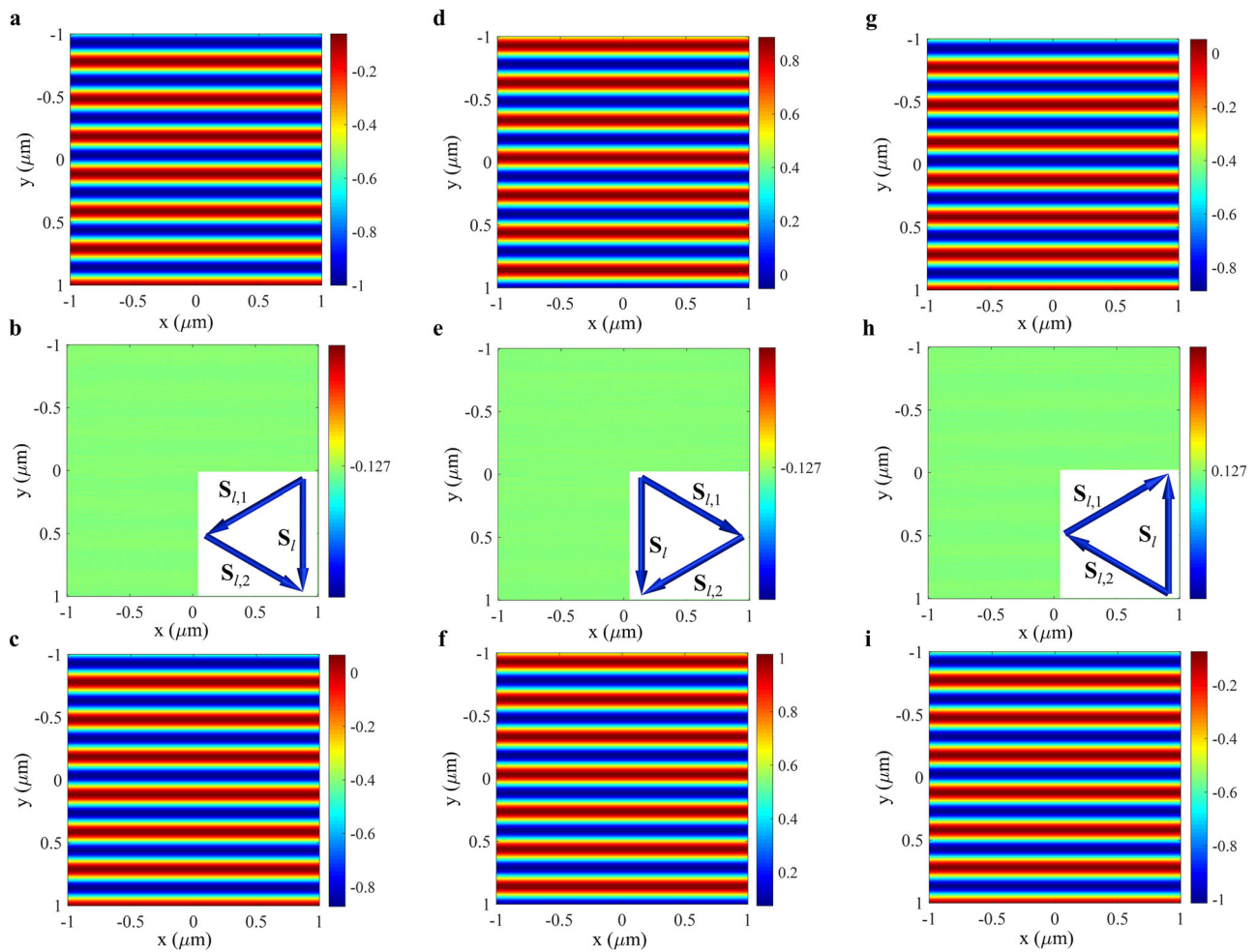
**Fig. 4 Momentum properties of the interference fields between two elliptically polarized evanescent waves.** **a** Schematic diagram of the interference between two evanescent waves carrying opposite helicities in the  $xy$ -plane. **b, c** The extracted helicity-unrelated and helicity-related  $x$ -component kinetic momentum when  $\theta = 45^\circ$ ,  $A_{s1} = 5 + 2i$  and  $A_{s2} = 5 - 2i$ . **d-f** Same as **(a-c)** but with  $\theta = 135^\circ$ . **g-i** Same as **(a-c)** but with opposite helicities, i.e.,  $A_{s1} = 5 - 2i$  and  $A_{s2} = 5 + 2i$ . In the calculation,  $A_{p1} = A_{p2} = 1$ ,  $k_p = 1.5k$ , and the wavelength of the waves is 632.8 nm.

free space by calculating the two-wave interference (Supplementary Note 3).

To understand in detail the spin property of an EM field, we first considered the interference of two waves with opposite helicities [Fig. 4(a)]. Thus, the coupling term  $\sigma_c$  vanishes and is thereby beneficial when analysing the spin property of EM fields. Assuming that  $A_{p1} = A_{p2} = 1$ ,  $A_{s1} = 5 + 2i$ ,  $A_{s2} = 5 - 2i$ , and that the propagating angles  $\theta$  of the two plane waves are  $+45^\circ$  and  $-45^\circ$ , the canonical momentum associated with the mean wavevector is along the  $+x$ -direction and varies periodically in the  $y$ -direction [Supplementary Fig. 2(b)]. The kinetic momentum [Supplementary Fig. 2(a)] has two components: the helicity-unrelated component along the  $+x$ -direction and varying periodically in the  $y$ -direction [Fig. 4(b)] and the helicity-related component along the  $-x$ -direction and being homogeneous in the  $xy$ -plane [Fig. 4(c)]. All the momenta decay exponentially in the  $z$ -direction. In this instance, the  $x$ -component SAM is absent, and only the  $z$ - and  $y$ -components of the SAM arise [Supplementary Fig. 3(a) and Fig. 5(a) in main text, respectively]. From our theory, the  $z$ -component SAM is a pure helicity-independent T-spin because the helicity-related kinetic momentum is spatially invariant in the  $xy$ -plane, whereas the  $y$ -component SAM contains both an L-spin and T-spin [Fig. 5(b, c), respectively].

To verify this, we then considered the interference of these two waves by changing the propagating angles to  $+135^\circ$  and  $-135^\circ$

[Fig. 4(d)] so that the propagating direction given by the canonical momentum [Supplementary Fig. 2(d)] is opposite to that given in Supplementary Fig. 2(b). The helicity-unrelated kinetic momentum is inverted [Fig. 4(e)], whereas the helicity-related kinetic momentum remains unchanged [Fig. 4(f)]. Thus, we found that the  $z$ -component of the SAM in Supplementary Fig. 3(f) is exactly inverted to that in Supplementary Fig. 3(a). This is a manifestation of the spin-momentum locking of the helicity-independent T-spin. The L-spin present in the  $y$ -component of the SAM [Fig. 5(d)] can be determined from a vector analysis based on Eq. (2). The identity of the spins in Fig. 5(b, e) demonstrates that the L-spin is independent of the propagating direction given by the canonical momentum and does not possess the spin-momentum locking property. The result found by subtracting the L-spins from the overall  $y$ -component of the SAMs thus yields the properties of the T-spin [Fig. 5(f)]. Moreover, the variation in the colour bar values in Fig. 5(e, f) indicates that the resultant T-spins should contain both helicity-independent and helicity-dependent T-spins because a pure helicity-independent T-spin is reversed exactly when the propagation direction is reversed. From Eq. (3), the helicity-independent  $y$ -component of T-spins [Supplementary Fig. 3(c, h)] was generated through the decay of the helicity-unrelated kinetic momentum [Fig. 4(b, e)] along the  $z$ -direction and was opposite when reversing the propagating direction of the field. In contrast, the  $y$ -component helicity-dependent T-spins



**Fig. 5 Spin properties of the interference fields between two elliptically polarized evanescent waves.** **a** Spatial distribution of the  $y$ -components of the SAM when  $\theta = 45^\circ$ ,  $A_{s1} = 5 + 2i$  and  $A_{s2} = 5 - 2i$ . **b** Extracted L-spin from the  $y$ -component of the SAM. The inset shows the vector decomposition. **c** The remaining T-spin for the  $y$ -component of the SAM. **d-f** Same as (a-c) but with  $\theta = 135^\circ$ . **g-i** Same as (a-c) but with opposite helicities, i.e.,  $A_{s1} = 5 - 2i$  and  $A_{s2} = 5 + 2i$ . In the calculation,  $A_{p1} = A_{p2} = 1$ ,  $k_p = 1.5k$ , and the wavelength of the waves is 632.8 nm.

[Supplementary Fig. 3(d, i)] are induced by the helicity-related component of kinetic momenta [Fig. 4(c, f)], which, although invariant in the  $xy$ -plane, decays in the  $z$ -direction. The helicity-dependent T-spins remain unchanged when changing the propagating direction because the helicity-related kinetic momentum remains unchanged.

Furthermore, to illustrate the helicity-dependent property of the EM spins, we considered the interference of two waves exchanging their helical properties [Fig. 4(g)]. In this instance, the direction of the canonical momentum [Supplementary Fig. 2(f)] is similar to that in Supplementary Fig. 2(b) except for a translation in the  $y$ -direction. Here, we shifted the calculation region of the SAMs to eliminate the effect of this translation. Compared with the case in Fig. 4(a), the helicity-unrelated kinetic momentum remains unchanged [Fig. 4(h)], whereas the helicity-related kinetic momentum is reversed [Fig. 4(i)]. Thus, the helicity-independent T-spin in Supplementary Fig. 3(k) is the same as that in Supplementary Fig. 3(a), whereas the L-spin in Fig. 5(h) from the vector analysis is inverted to that in Fig. 5(b). By subtracting the L-spins from the  $y$ -component of the SAM [Fig. 5(g)], we obtained the T-spin in the  $y$ -direction [Fig. 5(i)] as well as the corresponding extracted helicity-independent and helicity-dependent T-spins [Supplementary Fig. 3(m, n)]. Under this circumstance, the helicity-independent T-spin remains unchanged, whereas the helicity-dependent T-spin is reversed.

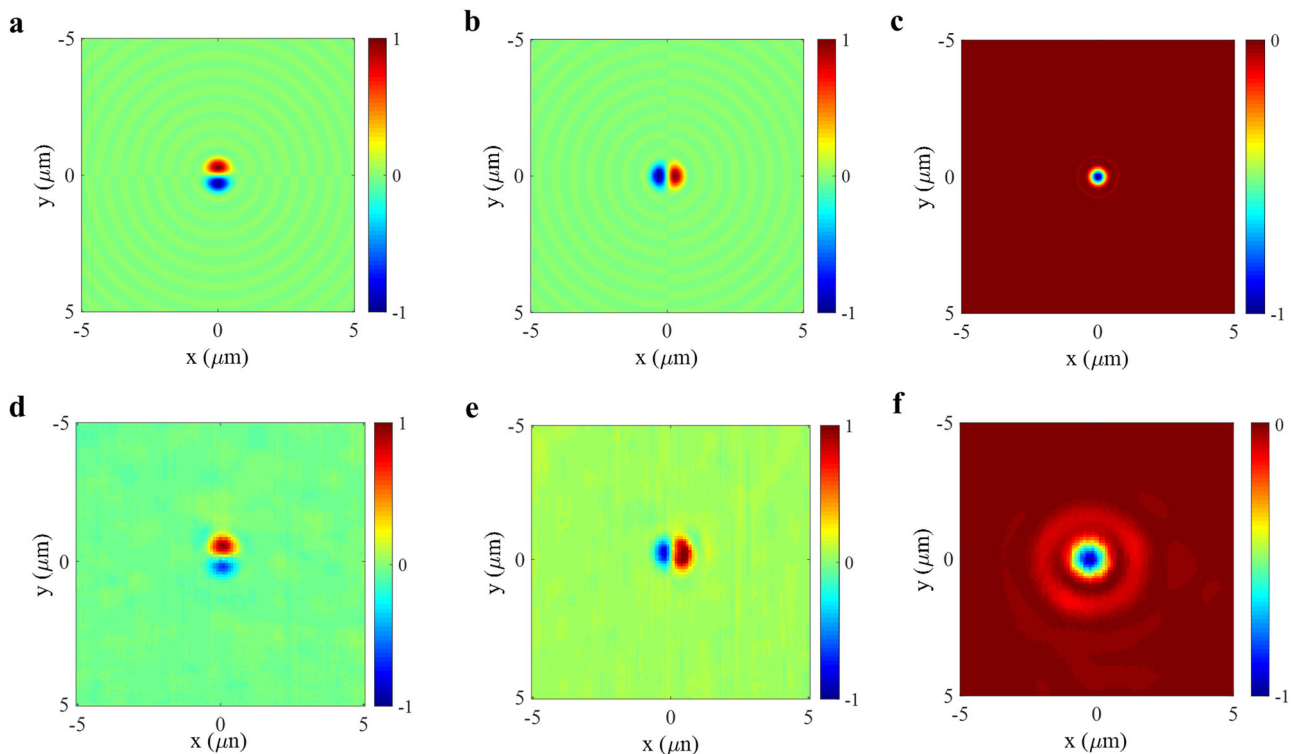
**Table 1 Classifications of physical properties of the T-spins and L-spins in a generic EM field.**

Classifications	Spin-momentum locking?	Helicity-dependent?
L-spin	No	Yes
Helicity-dependent T-spin	Yes	Yes
Helicity-independent T-spin	Yes	No

The classifications of EM spins into T-spins and L-spin are based on their spin-momentum locking and helicity-dependent properties. By decomposing the EM field into the superposition of plane waves, we derive that the L-spins are associated with the EM helicity whereas the T-spins possess the spin-momentum locking properties universally (Eq. (2) and Eq. (3)).

For a clear comparison, we summarized the primary properties of these three types of EM spins in Table 1.

**Helicity-dependent transverse spin and Berry curvature.** The T-spin is closely related to the Berry curvature of an optical system. For a linearly polarized EM field, the kinetic momentum is expressed as  $\Pi \propto \langle \Psi | i \nabla | \Psi \rangle$ , with  $|\Psi\rangle$  representing the potential<sup>54</sup>. The T-spin is then given by  $S_t \propto \nabla \times \Pi \propto \langle \nabla \Psi | \times i | \nabla \Psi \rangle$ , which has a similar form to the



**Fig. 6 Experimental validation of the T-spin and spin-momentum locking in a focused circularly polarized beam (CPB).** **a–c** Theoretically calculated  $y$ -,  $z$ - and  $x$ -components, respectively, of the SAM densities of a focused LCP beam. **d–f** Corresponding experimental results. The corresponding theoretical and experimental results for the focused RCP beam can be found detailedly in Supplementary Fig. 8 and Fig. 10. The optical axis is along the  $x$ -direction. Since the incident beam is changed from LCP to RCP, the  $y$ - and  $z$ -components of the SAM remain unchanged, thereby manifesting a helicity-independent T-spin. In contrast, the sign of the  $x$ -component of the SAM changes from positive to negative. This spin component contains two parts: the L-spin and the helicity-dependent T-spin. Together with the inverted propagating property, the T-spin of the focused circularly polarized light was demonstrated to possess  $\mathbb{Z}_4$  topological invariance, which matches well with the theoretical analysis.

Berry curvature of the potential<sup>2,16,38</sup>. Moreover, for a generic EM field, the T-spin determined by  $\nabla \times \mathbf{\Pi}$  also has a similar structure as the quantum 2-form<sup>55</sup> that generates the Berry phase associated with a circuit in real space (Supplementary Note 4). For a linearly polarized EM field, the circulation integral of the Berry curvature defining the geometric phase vanishes, and thus, the helicity-independent T-spin is unrelated to the geometric phase. However, from Eq. 7, the helicity-dependent T-spin is found to be antiparallel to the local wavevector in a general EM field. This is indeed a general property of the helicity-dependent T-spin and widely exists in a generic EM field. Previously, the generation of this inverted helical component was explained based on the evolution of the geometric phase in EM systems<sup>2,27</sup>. This may reveal that the helicity-dependent T-spin is closely related to the evolution of the geometric phase in EM systems such as focused CP beams (Supplementary Note 5). Based on the former considerations, we formulated four Maxwell-like spin-momentum equations and a Helmholtz-like equation in Supplementary Note 4 that can be utilized to analyse the spin-orbit coupling properties for general EM fields.

**Experimental demonstrations of the properties of the EM spins.** After establishing the unified spin-based field theory for general EM fields, we can utilize this field theory to construct topological spin quasiparticles. For example, for the linearly polarized surface wave at the air/metal interface, the cylindrically symmetric mode excited by circularly polarized light only possesses azimuthal kinetic momentum, and this kinetic momentum is helicity-unrelated. Therefore, from Eq. (3), the gradient of the azimuthal kinetic momentum in the normal direction leads to the

radial SAM, and the gradient of azimuthal kinetic momentum in the radial direction results in the SAM in the normal direction, which is a manifestation of a Néel-type spin skyrmion<sup>20</sup>. On the other hand, for the focused field of circularly polarized light in free space, there are two kinetic momentum components in the axial and azimuthal directions. The gradient of the axial kinetic momentum in the azimuthal direction is zero due to the cylindrical symmetry of the EM field, and the gradient of the axial kinetic momentum in the radial direction leads to the azimuthal T-spin. Moreover, the gradient of the azimuthal kinetic momentum in the axial direction is zero in the focal plane, and the gradient of azimuthal kinetic momentum in the radial direction leads to an axial T-spin. The combination of this axial T-spin and L-spin constitutes the total SAM component in the axial direction. Overall, the presence of SAMs in the azimuthal and axial directions produces Bloch-type spin skyrmions.

Finally, to validate the above intriguing topological properties of EM spins, we built a scanning imaging system to map the three SAM components for optical spin skyrmions by focused CP light propagating in the  $x$ -direction (Supplementary Note 6). Figure 6(a, b) exhibit the theoretical calculated results of  $S_y$  and  $S_z$  for left-handed circular polarization (LCP) focused light, and the corresponding experimental results are shown in Fig. 6(d, e) (The theoretical and experimental results of the right-handed circular polarization (RCP) can be found in Supplementary Fig. 8). The experimental results match well with the theoretically calculated results and reveal that these two SAM components of a focused field remain unchanged when the incident light is converted from LCP to RCP. These results correspond to the helicity-independent T-spin. Moreover, through the coordinate transformation, we can



**Table 2 The dynamical and topological properties of generic EM wave, linear polarized surface EM wave, deep-water gravity wave, and acoustic wave fields.**

	Generic EM wave	Linear polarized surface EM wave	Gravity water wave	Acoustic wave
Field components	Electric field $\mathbf{E}$ ; Magnetic field $\mathbf{H}$ ;	Electric or magnetic Hertz potential $\Psi$ ;	In-plane velocity $\mathbf{V}$ ; Normal velocity $W$ ;	Velocity $\mathbf{v}$ ; Pressure $p$ ;
Kinetic momentum	$\mathbf{\Pi} = \frac{1}{2c^2} \text{Re}\{\mathbf{E}^* \times \mathbf{H}\}$	$\mathbf{\Pi} = \frac{ek^2 k_z^2}{2\omega} \text{Im}\{\Psi^* \nabla \Psi\}$	$\mathbf{\Pi}_G = \frac{\rho_G k_G}{\omega_G} \text{Im}\{W^* \mathbf{V}\}$	$\mathbf{\Pi}_A = \frac{1}{2c_A^2} \text{Re}\{p^* \mathbf{v}\}$
Spin angular momentum	$\mathbf{S} = \frac{1}{4\omega} \text{Im}\left\{ \begin{matrix} \epsilon \mathbf{E}^* \times \mathbf{E} \\ + \mu \mathbf{H}^* \times \mathbf{H} \end{matrix} \right\}$	$\mathbf{S} = \frac{ek^2 k_z^2}{4\omega} \text{Im}\{\nabla \Psi^* \times \nabla \Psi\}$	$\mathbf{S}_G = \frac{\rho_G}{2\omega_G} \text{Im}\{\mathbf{V}^* \times \mathbf{V}\}$	$\mathbf{S}_A = \frac{\rho_A}{2\omega_A} \text{Im}\{\mathbf{v}^* \times \mathbf{v}\}$
Helicity	Spin-1 photon $\sigma = \pm 1$	Spin-1 photon $\sigma = \pm 1$	Spin-0 phonon $\sigma_G = 0$	Spin-0 phonon $\sigma_A = 0$
Spin-momentum locking	$\mathbf{S}_t = \frac{1}{2k^2} \nabla \times \mathbf{\Pi}$ $\mathbf{S}_l = \sum_i \hbar \sigma_i \hat{\mathbf{k}}_i + \sum_{i \neq j} \hbar \sigma_{ij} \hat{\mathbf{k}}_{ij}$	$\mathbf{S}_t = \frac{1}{2k^2} \nabla \times \mathbf{\Pi}$ $\mathbf{S}_l = 0$	$\mathbf{S}_G = \frac{1}{2k_G^2} \nabla_2 \times \mathbf{\Pi}_G$	$\mathbf{S}_A = \frac{1}{k_A^2} \nabla \times \mathbf{\Pi}_A$

The field, kinetic momentum, SAM, helicity and spin-momentum locking properties of general EM field, linear polarized surface EM field, gravity water waves and acoustic waves. Therein, the field, kinetic momentum and SAM properties can be found in Ref. 6 and the Supplementary Table. S1 of Ref. 15, respectively. For the longitudinal acoustic wave,  $c_A^2 = 1/\beta_A \rho_A$  is the speed of the acoustic wave, where  $\beta_A$  is the compressibility of the acoustic medium;  $\rho_A$  is the mass density of the acoustic medium;  $\omega_A$  and  $k_A = \omega_A/c_A$  are the angular frequency and wavenumber, respectively;  $\sigma_W = 0$  for the phonons corresponding to the longitudinal acoustic waves; and  $\rho_G$  is the mass density of the fluid.

find that the combination of  $S_y$  and  $S_z$  results in the azimuthal SAM  $S_\phi$  (the small radial SAM component originates from the experimental errors). On the other hand, Fig. 6(c) exhibit the theoretically calculated result of the axial SAM for focused LCP light and the corresponding experimental result is given by Fig. 6(f) (The theoretical and experimental results of the right-handed circular polarization (RCP) can be found in Supplementary Fig. 11). From the experimental results, we observed that the  $x$ -component SAMs are helicity-dependent and inverted when the incident light is converted from LCP to RCP. As analysed above, the  $x$ -components of SAM contain both L-spins and helicity-dependent T-spins. From the experimental results, we can find that the azimuthal and axial SAM densities exist in the focusing field, which is a manifestation of Bloch-type spin skyrmions. In addition, by further considering the reversal of the propagation direction, four momentum-locked T-spin states are found in the focused CP light systems, which is consistent with the nontrivial spin Chern number of an optical wave packet and reveals that these T spins possess  $\mathbb{Z}_4$  topological invariance<sup>13,17</sup>.

### Discussions and conclusions

To summarize, we derived a unified theory that involves the decomposition of EM spin and uncovered the underlying physical difference between T-spins and L-spins. L-spins are determined by the EM helicity, but coupling effects need to be considered. However, T-spins originate from the spatial inhomogeneity of the kinetic momentum density and undergo universal spin-momentum locking. Here, we emphasize that the T-spin is locked with the kinetic momentum rather than with the canonical momentum given by the mean wavevector. Indeed, T-spins can be oriented parallel to the mean wavevector. Furthermore, T-spins decompose into helicity-independent and helicity-dependent components, which are determined separately by the vorticities of a helicity-unrelated and a helicity-related kinetic momentum. Thus, four spin-momentum locking states exist, with the number being consistent with the nontrivial topological spin Chern number. Moreover, the T-spin bearing the curl-relationship with the kinetic momentum is closely related to the Berry curvature of an EM system. Specifically, the helicity-dependent T-spin, which is associated with the inverted helical component, can be explained based on the evolution of the geometric phase in EM systems.

The spin angular momentum density of the EM field given in Eq. (2) and Eq. (3) can be considered the local behaviour of many photons. To understand the global behaviour of photons, we employed the integral of the spin angular momentum density on the two-dimensional transverse plane. Regarding physical reality,

the EM field is bounded (decaying to zero at infinity), and the integral of T-spin on the transverse plane is

$$\iint_{\infty} \mathbf{S}_t d^2 \mathbf{r}_{\perp} = \iint_{\infty} \frac{1}{2k^2} \nabla \times \mathbf{\Pi} d^2 \mathbf{r}_{\perp} = \frac{1}{2k^2} \oint_{\infty} \mathbf{\Pi} dl = 0. \tag{16}$$

The integral of L-spin on the transverse plane is

$$\left| \iint_{\infty} \mathbf{S}_l d^2 \mathbf{r}_{\perp} \right| = \left| \iint_{\infty} \left[ \sum_i \hbar \sigma_i \hat{\mathbf{k}}_i + \sum_{i \neq j} \hbar \sigma_{ij} \hat{\mathbf{k}}_{ij} \right] d^2 \mathbf{r}_{\perp} \right| \tag{17}$$

$$= \sum_i \hbar \sigma_i \iint_{\infty} \frac{W_i}{k\omega} d^2 \mathbf{r}_{\perp}.$$

Here,  $\iint_{\infty} \frac{W_i}{k\omega} d^2 \mathbf{r}_{\perp}$  is evaluated to obtain the number of photons.  $\mathbf{r}_{\perp}$  represents the coordinates in the transverse plane, and the integral boundary of the transverse plane is infinite. Therefore, although the photons suffer from spin-orbit couplings, the integral properties of photons remain unchanged in a homogeneous space.

Our theory has an interdisciplinary impact and is extendible to other classical wave fields. For example, the spin-momentum locking relationship of the longitudinal acoustic wave (identified with Subscript A) can be expressed as  $\mathbf{S}_A = \mathbf{\Pi}_A/k_A^2$ <sup>15</sup>, where  $\mathbf{S}_A$  and  $\mathbf{\Pi}_A$  are the total SAM and kinetic momentum of a monochromatic time-harmonic acoustic wave, respectively. Now, we demonstrate that for a deep-water gravity wave (identified with Subscript G)<sup>6</sup>, a similar spin-momentum relationship  $\mathbf{S}_G = \nabla_2 \mathbf{\Pi}_G/2k_G^2$  is valid. This relation reveals that the SAM of a surface water wave is locked with the kinetic momentum and obeys the right-hand rule and that the total SAM may be considered the T-spin. Here,  $\mathbf{S}_G$  and  $\mathbf{\Pi}_G$  are the total SAM and kinetic momentum, respectively, of monochromatic time-harmonic gravity water waves;  $\nabla_2 = (\partial_x, \partial_y)$ ;  $\omega_G^2 = gk_G$  with  $\omega_G$  and  $k_G$  being the angular frequency and wavenumber of the water wave; and  $g$  denotes the gravitational acceleration. We note that longitudinal spin is absent because longitudinal acoustic waves ( $\sigma_A = 0$ ) and surface water waves ( $\sigma_G = 0$ ) can be considered spin-0 phonons. These results reveal the physical origins and topological properties of spin in diverse classical wave fields and illuminate the universality of spin-momentum locking. They motivate explorations of field theory based on spin degrees of freedom and constructions of chiral spin textures<sup>56,57</sup>. For a clear comparison, we summarized the primary dynamic properties of diverse types of wave fields in Table 2.

For applications, this spin-momentum locking property of T-spin in a generic EM field can be utilized to construct diverse photonic topological spin structures, such as Néel-type skyrmions

in confined EM fields and Bloch-type skyrmions in free space. Moreover, we performed numerical simulations (Supplementary Note 7) to demonstrate the properties of momentum-locked transverse optical forces by considering the interactions between metallic helical nanostructures and Bloch-type skyrmions in free space. These simulations suggest further applications in chiral sorting using photonic topological spin structures. Overall, the findings reveal a unified field theory to describe the spin-orbit coupling of light based on the spin degrees of freedom and wave-matter interactions in interdisciplinary research and motivate explorations of applications in optical manipulation, chiral quantum optics, and electronics<sup>58,59</sup>.

## Methods

**Experimental details.** The experimental setup for mapping the SAM components perpendicular to the optical axis (Supplementary Fig. 6) comprises an incident beam (wavelength: 632.8 nm) that is tightly focused by an objective lens (Olympus, NA = 0.5, 50×) onto a PS nanoparticle (diameter: 201 nm) sitting on a silver film (thickness: 45 nm). The focusing field and the scattering field of the PS particle (the far-field radiation field and part of the near-field evanescent field) radiate downward by coupling with the silver film. The signal was collected by an oil-immersed objective lens (Olympus, NA = 1.49, 100×). Using a high-precision piezo-stage (Physik Instrumente, P-545), we moved the PS particle through the focal plane of the tightly focused beam. Each time the position is moved, the back focal plane intensity (far-field intensity) distribution is imaged using a four-quadrant detector. From dipole theory and similar techniques described in Ref. 13, the transverse components of the SAM density can be reconstructed.

The setup of the tip-fibre-based measurement system that maps the SAM component parallel to the optical axis (Supplementary Fig. 9) comprises a He-Ne laser (operating wavelength: 632.8 nm) used as a light source. The light beam is expanded and collimated via a telescope system and then passed through a linear polarizer (LP) and a quarter wave plate (QWP) to produce the desired LCP or RCP light. The beam is then focused using an objective lens (Olympus, NA 0.7, 60×) onto a silica coverslip for further image scanning by a self-assembly near-field scanning optical microscopic system. The system's probe has a nanohole and is controlled using a tuning fork feedback system for mapping the in-plane field distributions of the focused beams. The near-field signal, which couples via the nanohole to the fibre, is split and then analysed using a combination of QWP and LP to extract the individual circular polarization components of the signal ( $I_{LCP}$ : LCP component and  $I_{RCP}$ : RCP component). These components are then directed to two photomultiplier tubes (PMTs) to measure the intensity of the two signals. This then enables a quantification of the out-of-plane SAM component (i.e., along the optical axis) of the focused beams using the relation

$$S_z = \frac{\varepsilon}{4\omega} \frac{k^2 + \kappa^2}{\kappa^2} (I_{RCP} - I_{LCP}). \quad (18)$$

## Data availability

The data that support the findings of this study are available from the corresponding author upon reasonable request.

Received: 22 February 2023; Accepted: 6 September 2023;

Published online: 05 October 2023

## References

- Fert, A. Nobel Lecture: Origin, development, and future of spintronics. *Rev. Mod. Phys.* **80**, 1517–1530 (2004).
- Bliokh, K. Y., Rodríguez-Fortuño, F. J., Nori, F. & Zayats, A. V. Spin-orbit interactions of light. *Nat. Photon* **9**, 796–808 (2015).
- Yuan, W. et al. Observation of elastic spin with chiral meta-sources. *Nat. Commun.* **12**, 6954 (2021).
- Wang, S. et al. Spin-orbit interactions of transverse sound. *Nat. Commun.* **12**, 6125 (2021).
- Long, Y., Ren, J. & Chen, H. Intrinsic spin of elastic waves. *Proc. Natl Acad. Sci. USA* **115**, 9951–9955 (2018).
- Bliokh, K. Y., Punzmann, H., Xia, H., Nori, F. & Shats, M. Field theory spin and momentum in water waves. *Sci. Adv.* **8**, abm1295 (2022).
- Xin, S., Long, Y. & Ren, J. Spin angular momentum of gravitational wave interference. *N. J. Phys.* **23**, 043035 (2021).
- Aiello, A., Banzer, P., Neugebauer, M. & Leuchs, G. From transverse angular momentum to photonic wheels. *Nat. Photon* **9**, 789–795 (2015).
- Neugebauer, M., Bauer, T., Aiello, A. & Banzer, P. Measuring the transverse spin density of light. *Phys. Rev. Lett.* **114**, 063901 (2015).
- Neugebauer, M., Eismann, J. S., Bauer, T. & Banzer, P. Magnetic and electric transverse spin density of spatially confined light. *Phys. Rev. X* **8**, 021042 (2018).
- Bekshaev, A. Y., Bliokh, K. Y. & Nori, F. Transverse spin and momentum in two-wave interference. *Phys. Rev. X* **5**, 011039 (2015).
- Bliokh, K. Y., Bekshaev, A. & Nori, F. Extraordinary momentum and spin in evanescent waves. *Nat. Commun.* **5**, 3300 (2014).
- Bliokh, K. Y., Smirnova, D. & Nori, F. Quantum spin Hall effect of light. *Science* **348**, 1448–1451 (2015).
- Van Mechelen, T. & Jacob, Z. Universal spin-momentum locking of evanescent waves. *Optica* **3**, 118–126 (2016).
- Shi, P., Du, L. & Yuan, X. Strong spin-orbit interaction of photonic skyrmions at the general optical interface. *Nanophotonics* **9**, 4619–4628 (2020).
- Shi, P. et al. Intrinsic spin-momentum dynamics of surface electromagnetic waves in dispersive interfaces. *Phys. Rev. Lett.* **128**, 218904 (2022).
- Shi, P., Du, L., Li, C., Zayats, A. V. & Yuan, X. Transverse spin dynamics in structured electromagnetic guided waves. *Proc. Natl Acad. Sci. USA* **118**, e2018816118 (2021).
- Shen, Y. et al. Optical vortices 30 years on: OAM manipulation from topological charge to multiple singularities. *Light Sci. Appl.* **8**, 90 (2019).
- Eismann, J. S. et al. Transverse spinning of unpolarized light. *Nat. Photon* **15**, 156–161 (2020).
- Dai, Y. et al. Plasmonic topological quasiparticle on the nanometre and femtosecond scales. *Nature* **588**, 616–619 (2020).
- Du, L., Yang, A., Zayats, A. V. & Yuan, X. Deep-subwavelength features of photonic skyrmions in a confined electromagnetic field with orbital angular momentum. *Nat. Phys.* **15**, 650–654 (2019).
- Tsesses, S., Cohen, K., Ostrovsky, E., Gjonaj, B. & Bartal, G. Spin-orbit interaction of light in plasmonic lattices. *Nano Lett.* **19**, 4010–4016 (2019).
- Lei, X. et al. Photonic spin lattices: symmetry constraints for skyrmion and meron topologies. *Phys. Rev. Lett.* **127**, 237403 (2021).
- Ghosh, A. et al. A topological lattice of plasmonic merons. *Appl. Phys. Rev.* **8**, 041413 (2021).
- Dai, Y. et al. Ultrafast microscopy of a twisted plasmonic spin skyrmion. *Appl. Phys. Rev.* **9**, 011420 (2022).
- Shi, P., Du, L. & Yuan, X. Spin photonics: from transverse spin to photonic skyrmions. *Nanophotonics* **10**, 3927–3943 (2021).
- Shi, P. et al. Optical near-field measurement for spin-orbit interaction of light. *Prog. Quantum Electron.* **78**, 100341 (2021).
- Bliokh, K. Y. & Nori, F. Transverse and longitudinal angular momenta of light. *Phys. Rep.* **592**, 1–38 (2015).
- Antognozzi, M. et al. Direct measurements of the extraordinary optical momentum and transverse spin-dependent force using a nano-cantilever. *Nat. Phys.* **12**, 731–735 (2016).
- Rodríguez-Fortuño, F. J. et al. Near-field interference for the unidirectional excitation of electromagnetic guided modes. *Science* **340**, 328–330 (2013).
- Petersen, J., Volz, J. & Rauschenbeutel, A. Chiral nanophotonic waveguide interface based on spin-orbit interaction of light. *Science* **346**, 67–71 (2014).
- Söllner, I. et al. Deterministic photon-emitter coupling in chiral photonic circuits. *Nat. Nanotech.* **10**, 775–778 (2015).
- Guo, Z., Long, Y., Jiang, H., Ren, J. & Chen, H. Anomalous unidirectional excitation of high-k hyperbolic modes using all-electric metasources. *Adv. Photon.* **3**, 036001 (2021).
- Araneda, G. et al. Wavelength-scale errors in optical localization due to spin-orbit coupling of light. *Nat. Phys.* **15**, 17–21 (2019).
- Zhou, J. et al. Metasurface enabled quantum edge detection. *Sci. Adv.* **6**, eabc4385 (2020).
- Zhou, J. et al. Optical edge detection based on high-efficiency dielectric metasurface. *Proc. Natl Acad. Sci. USA* **116**, 11137–11140 (2019).

37. Yang, A. et al. Spin-manipulated photonic skyrmion-pair for pico-metric displacement sensing. *Adv. Sci.* **10**, 2205249 (2023).
38. Lei, X., Du, L., Yuan, X. & Zayats, A. V. Optical spin-orbit coupling in the presence of magnetization: photonic skyrmion interaction with magnetic domains. *Nanophotonics* **10**, 3667–3675 (2021).
39. Lodahl, P. et al. Chiral quantum optics. *Nature* **541**, 473–480 (2017).
40. Forbes, A., de Oliveira, M. & Dennis, M. R. Structured light. *Nat. Photon.* **15**, 253–262 (2021).
41. Sakurai, J. J. *Modern Quantum Mechanics* (Addison-Wesley, San Francisco, CA, 1994).
42. Alpeggiani, F., Bliokh, K. Y., Nori, F. & Kuipers, L. Electromagnetic helicity in complex media. *Phys. Rev. Lett.* **120**, 243605 (2018).
43. Bliokh, K. Y., Bekshaev, A. Y. & Nori, F. Optical momentum, spin, and angular momentum in dispersive media. *Phys. Rev. Lett.* **119**, 073901 (2017).
44. Kemp, B. A. Resolution of the Abraham-Minkowski debate: Implications for the electromagnetic wave theory of light in matter. *J. Appl. Phys.* **109**, 111101 (2011).
45. Pfeifer, Robert N. C., Nieminen, T. A., Heckenberg, N. R. & Rubinsztein-Dunlop, H. Colloquium: Momentum of an electromagnetic wave in dielectric media. *Rev. Mod. Phys.* **79**, 1197–1216 (2007).
46. Berry, M. V. Optical currents. *J. Opt. Pure Appl. Opt.* **11**, 094001 (2009).
47. Shi, P., Du, L., Li, M. & Yuan, X. Symmetry-protected photonic chiral spin textures by spin-orbit coupling. *Laser Photonics Rev.* **15**, 2000554 (2021).
48. Li, M. et al. Orbit-induced localized spin angular momentum in strong focusing of optical vectorial vortex beams. *Phys. Rev. A* **97**, 053842 (2018).
49. Yu, P., Zhao, Q., Hu, X., Li, Y. & Gong, L. Orbit-induced localized spin angular momentum in the tight focusing of linearly polarized vortex beams. *Opt. Lett.* **43**, 5677–5680 (2018).
50. Forbes, K. A. & Jones, G. A. Measures of helicity and chirality of optical vortex beams. *J. Opt.* **23**, 115401 (2021).
51. Barnett, S. M., Cameron, R. P. & Yao, A. M. Duplex symmetry and its relation to the conservation of optical helicity. *Phys. Rev. A* **86**, 013845 (2012).
52. Kane, C. L. & Mele, E. J. Z<sub>2</sub> topological order and the quantum spin Hall effect. *Phys. Rev. Lett.* **95**, 146802 (2005).
53. Fernandez-Corbaton, I. et al. Electromagnetic duality symmetry and helicity conservation for the macroscopic Maxwell's equations. *Phys. Rev. Lett.* **111**, 060401 (2013).
54. Wolf, E. A scalar representation of electromagnetic fields: II. *Proc. Phys. Soc.* **74**, 269–280 (1959).
55. Berry, M. V. Quantal phase factors accompanying adiabatic changes. *Proc. R. Soc. A* **392**, 45–57 (1984).
56. Muelas-Hurtado, R. D. et al. Observation of polarization singularities and topological textures in sound waves. *Phys. Rev. Lett.* **129**, 1–6 (2022).
57. Ge, H. et al. Observation of acoustic skyrmions. *Phys. Rev. Lett.* **127**, 144502 (2021).
58. Ni, J. et al. Gigantic vortical differential scattering as monochromatic probe for multiscale chiral structures. *Proc. Natl Acad. Sci. USA* **118**, e20200551 (2021).
59. Chen, Y. et al. Multidimensional nanoscopic chiroptics. *Nat. Rev. Phys.* **4**, 113 (2022).

## Acknowledgements

This work was supported, in part, by the Guangdong Major Project of Basic Research grant 2020B0301030009, the National Natural Science Foundation of China grants 12174266, 92250304, 61935013, 62075139, 61427819, 61622504, the Leadership of Guangdong province programme grant 00201505, and the Science and Technology Innovation Commission of Shenzhen grants JCYJ20200109114018750.

## Author contributions

P.S. conceived the concept, performed the theory. A.Y. and X.Y. performed the experiments. P.S., L.D. and X.L. analyzed the data and wrote the draft. P.S., L.D. and X.Y. revised the draft and supervised the work.

## Competing interests

The authors declare no competing interests.

## Additional information

**Supplementary information** The online version contains supplementary material available at <https://doi.org/10.1038/s42005-023-01374-y>.

**Correspondence** and requests for materials should be addressed to Peng Shi, Luping Du or Xiaocong Yuan.

**Peer review information** *Communications Physics* thanks Sebastian Golat, Hadiseh Alaeian and the other, anonymous, reviewer(s) for their contribution to the peer review of this work. A peer review file is available.

**Reprints and permission information** is available at <http://www.nature.com/reprints>

**Publisher's note** Springer Nature remains neutral with regard to jurisdictional claims in published maps and institutional affiliations.



**Open Access** This article is licensed under a Creative Commons Attribution 4.0 International License, which permits use, sharing, adaptation, distribution and reproduction in any medium or format, as long as you give appropriate credit to the original author(s) and the source, provide a link to the Creative Commons licence, and indicate if changes were made. The images or other third party material in this article are included in the article's Creative Commons licence, unless indicated otherwise in a credit line to the material. If material is not included in the article's Creative Commons licence and your intended use is not permitted by statutory regulation or exceeds the permitted use, you will need to obtain permission directly from the copyright holder. To view a copy of this licence, visit <http://creativecommons.org/licenses/by/4.0/>.

© The Author(s) 2023